

## The materials science beamline at the Swiss Light Source: design and realization

B.D. Patterson<sup>a,\*</sup>, R. Abela<sup>a</sup>, H. Auderset<sup>a</sup>, Q. Chen<sup>a</sup>, F. Fauth<sup>a,1</sup>,  
F. Gozzo<sup>a</sup>, G. Ingold<sup>a</sup>, H. Kühne<sup>a</sup>, M. Lange<sup>a</sup>, D. Maden<sup>a</sup>,  
D. Meister<sup>a</sup>, P. Pattison<sup>b</sup>, Th. Schmidt<sup>a</sup>, B. Schmitt<sup>a</sup>, C. Schulze-Briesse<sup>a</sup>,  
M. Shi<sup>a</sup>, M. Stampanoni<sup>a</sup>, P.R. Willmott<sup>a</sup>

<sup>a</sup>Swiss Light Source Project, Paul Scherrer Institute, WLG A 233, CH-5232 Villigen, Switzerland

<sup>b</sup>SNBL at ESRF, BP 220, F-38043 Grenoble Cedex 9, France

Received 1 October 2004; accepted 3 November 2004

Available online 16 December 2004

---

### Abstract

The Materials Science Beamline at the Swiss Light Source (SLS) has been designed to produce hard X-rays in the photon-energy range 5–40 keV, at an intermediate energy (2.4 GeV) synchrotron. To this end, it employs a novel “minigap wiggler”. Important issues in the design and realization of the beamline are the high heat load, robust system design, flexibility of operation and user-friendliness. A conventional collimating-mirror/sagittally focusing double-crystal monochromator/focusing mirror optics has been chosen with approximately 1:1 symmetry. Established component designs have been used wherever possible. Three serial end-stations are served with X-rays. Besides the minigap wiggler, other novel or unusual features are: continuous “top-up” injection in the SLS storage-ring, a rotating carbon “cup” filter in the beamline front-end, angles and bending radii of the optics mirrors which are adjusted at each change in photon-energy and special experimental-station equipment including high-speed one- and two-dimensional semiconductor detectors for powder and surface diffraction and a two-dimensional “Bragg magnifier” for tomography. In this work, a comparison is made between predicted and measured beamline properties, and Appendices with useful formulae and algorithms are provided.

© 2004 Elsevier B.V. All rights reserved.

PACS: 07.85.Qe; 41.50.+h; 61.10.-i; 87.59.-e

Keywords: Synchrotron radiation; Materials science; X-ray diffraction; Tomography

---

\*Corresponding author. Tel.: + +41 56 310 4524; fax: + +41 56 310 4551.

E-mail address: [bruce.patterson@psi.ch](mailto:bruce.patterson@psi.ch) (B.D. Patterson).

<sup>1</sup>Present address: European Synchrotron Radiation Facility, F-38043 Grenoble, France.

## 1. Introduction

The Swiss Light Source (SLS) [1], a third-generation synchrotron facility (2.4 GeV, 400 mA) at the Paul Scherrer Institute, began commissioning in 2001 with an initial set of four X-ray beamlines: two for soft-X-ray photoemission spectroscopy and microscopy and two for hard-X-ray diffraction and imaging. At the time of writing, six beamlines are in operation and another five are under construction or at advanced stages of planning. The hardest X-rays at the SLS (5–40 keV) are generated at the Materials Science (MS) Beamline (Fig. 1), where experimental stations are dedicated to X-ray tomographic microscopy (XTM) [2], powder diffraction (PDiff) [3] and in situ surface diffraction (SDiff) [4]. The beamline is presently available approximately 30 weeks per year for user operation.

The specifications of the beamline are presented in Table 1, and the positions along the beamline of the major components are given in Table 2. This work documents the design and performance of the beamline, describes several novel developments and provides some, hopefully useful, “tricks of the trade”. Section 2 summarizes the important features of the SLS storage-ring. The major pieces of the beamline source and optics are the minigap wiggler (Section 3), the “front-end” safety system (Section 4) and the X-ray optics (Section 5), and their performance is presented in Section 6. The experimental areas are briefly described in Section 7, a Summary and Conclusions are given in Section 8, and the Appendices provide a collection

of data and algorithms of use to the beamline designer.

## 2. The SLS storage ring

The designation of the SLS as a “third-generation” synchrotron source refers to the emphasis for radiation generation on insertion-devices (undulators

Table 1  
Materials science beamline specifications

Energy range	5–40 keV
Accepted divergence	$0.23 (v) \times 2.5 (h) \text{ mrad}^2$
Flux at 10 keV	$10^{13}$ photons/s
Energy resolution $\Delta E/E$	0.0139% (Si (1 1 1))
Focused spot size	$160 (v) \times 450 (h) \mu\text{m}^2$ FWHM

Table 2  
Positions of the major beamline components with respect to the center of the wiggler

Component	Distance (m)
Wiggler (W61)	0
Aperture	9.67
Rotating C-filter	12.14
Be windows	15.43
Collimating mirror (M1)	17.57
DCM: first crystal (X1)	19.54
DCM: second crystal (X2)	19.55–19.83
Focusing mirror (M2)	22.00
X-ray tomographic microscopy (XTM)	32.37
Powder diffractometer (PDiff)	36.10
Surface diffractometer (SDiff)	40.78

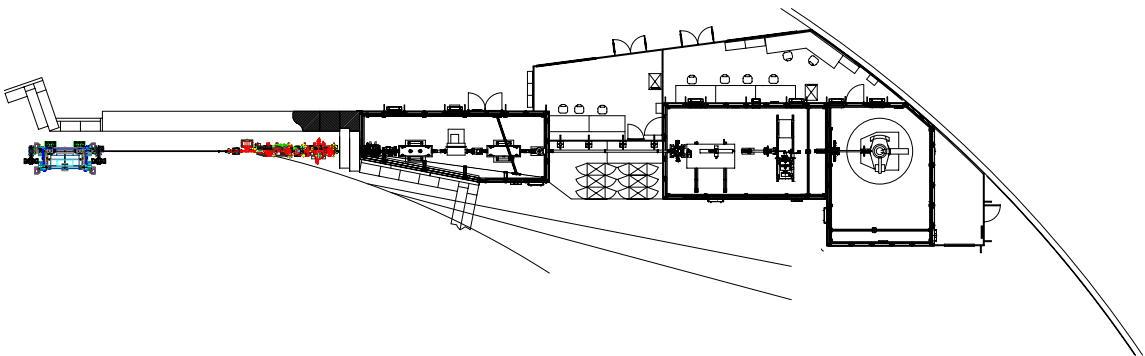


Fig. 1. The layout of the MS beamline.

Table 3  
SLS specifications

Linear accelerator	100 MeV
Booster synchrotron	2.4 GeV
Storage ring ( $E_e$ )	2.4 GeV
SLS circumference	288 m
Electron current ( $I_e$ )	300–400 mA
Vertical emittance	0.03 nm-radians
Number of electron bunches	480
Bunch length	43 ps
Relativistic electron mass ( $\gamma$ )	4697
Electron beam size (FWHM)	$18(v) \times 235(h) \mu\text{m}^2$

and wigglers), situated at numerous “straight sections”. Much emphasis is given to minimizing the cross-sectional size of the electron beam (high  $\beta$ -factor). This results in a low emittance and a high brightness (photons/time/bandwidth/source area/emission solid-angle) of the undulator beams. In addition, it allows the use of small-gap ( $\sim 5$  mm) insertion devices. The low emittance is less important for the wiggler source of the MS beamline, where the goal is a high photon flux (photons/time) or spectral flux (photons/time/bandwidth) into a reasonably small focus area and at high photon energy. Insertion devices can be placed in 9 of the 12 straight sections of the SLS.

Specifications of the SLS storage-ring are given in Table 3. The fact that injection from the booster synchrotron to the storage ring is performed at the full 2.4 GeV electron energy allows the realization of “top-up” operation, whereby small amounts of charge are injected at approximately 3 min intervals to keep the storage-ring current constant over days to within 1%. This feature is important for the beamline design, since the heat-load on the optics is essentially constant in time.

### 3. The W61 minigap-wiggler

#### 3.1. General description

A wiggler insertion device consists of a linear array of  $N$  oppositely poled magnet pairs (permanent or electromagnetic), which forces the electrons travelling along its central axis to follow an approximately sinusoidal path. The maximum field

is  $B_{\text{max}}$ , and the magnetic wavelength is  $\lambda_w$ . Radiation is emitted along the curved sections of this path, with characteristic opening angles of approximately  $1/\gamma$  and  $\delta$  in the vertical and horizontal directions, respectively, where  $\gamma$  is the ratio of the relativistic electron mass to the rest mass ( $\gamma = 4697$  for the SLS), and  $\delta$  is the maximum electron deflection angle. When the ratio

$$K \equiv \delta\gamma = \frac{eB_{\text{max}}\lambda_w}{2\pi mc} \quad (1)$$

is less than unity, the radiation from the individual poles of the insertion device interfere, and we have the case of an “undulator”. The photon-energy spectrum then consists of widely separated harmonic peaks, and the radiation cone subtends the reduced solid angle  $1/(nN\gamma^2)$ , where  $n$  is the harmonic number. As  $n$  increases, the intensity of the corresponding harmonic peak generally decreases due to the finite electron energy spread and emittance of the storage-ring and to phase errors in the undulator magnetic array.

For  $K$ -values much larger than unity (the MS beamline wiggler has  $K = 8.6$ ), the emitted radiation is mainly at high energies, and it takes on the characteristics of an incoherent sum of bending-magnet radiation from the  $N$  poles; the insertion device is now referred to as a “wiggler”. Although not as bright as that from an undulator, wiggler radiation has a continuous spectrum extending to high photon energies. In order to produce usable amounts of radiation above 20 keV, the MS-wiggler gap is kept small (hence the term “minigap” wiggler). The MS-wiggler has a minimum magnetic gap of 8 mm, within which an aluminum vacuum chamber is situated. The internal vacuum gap for the electron beam is 5 mm. Specifications of the MS minigap wiggler are presented in Table 4.

Other hard-X-ray beamlines at the SLS use “in-vacuum undulators” [5]. Here the Halbach-type hybrid magnet arrays [6] occupy the same ultra-high vacuum chamber as the electron beam, allowing a minimum gap of less than 5 mm. A similar approach for the MS-minigap-wiggler was rejected because of manpower constraints and the ready availability of suitable Al-profile for the minigap vacuum chambers [7]. The latter allowed the fabrication of three chambers, with 1 mm wall

Table 4  
Minigap wiggler specifications

Overall length ( $L_w$ )	2 m
Minimum magnetic gap ( $w$ )	8 mm
Period length ( $\lambda_w$ )	60.5 mm
Number of poles ( $N_p$ )	63
Magnet material	NdFe:B
Pole material	CoFe
Maximum field ( $B_{\max}$ )	1.84 T
Effective field ( $B_{\text{eff}}$ )	1.63 T
Fourier amplitude ratio ( $\eta = B_1/B_0$ )	-0.163
Deviation parameter ( $K$ )	8.6
Critical energy ( $E_c$ )	7.0 keV

thickness and outer dimensions of 14, 10 and 7 mm. As the SLS-operation improved, the gap was successively decreased.

### 3.2. Design and optimization

Details of the MS-wiggler design will be published elsewhere [5]. The analysis presented below, based on the algorithms of Tatchyn [8], was made at an early design stage. Tatchyn applies the standard formulae for synchrotron radiation emission from a bending magnet to the numerically determined path of an electron through the magnetic-field profile  $B(z)$ , where  $z$  is the coordinate along the wiggler axis. This involves expressing  $B(z)$ , which is periodic in the wiggler period  $\lambda_w$ , as a sine Fourier series:

$$B(z) = \sum_{n=0}^{\infty} B_n \sin \left[ \frac{2\pi(2n+1)z}{\lambda_w} \right]. \quad (2)$$

This has the maximum value:

$$B_{\max} = B \left( \frac{\lambda_w}{4} \right) = \sum_{n=0}^{\infty} (-1)^n B_n \quad (3)$$

and a mean-square value:

$$\langle B^2 \rangle = \frac{1}{\lambda_w} \int_0^{\lambda_w} B^2(z) dz = \frac{1}{2} \sum_{n=0}^{\infty} B_n^2 \equiv \frac{1}{2} B_{\text{eff}}^2 \quad (4)$$

where  $B_{\text{eff}}$  is known as the “effective” wiggler field. The total power emitted by the wiggler is given by [9]

$$P[\text{kW}] = 1.27 E_c^2 [\text{GeV}^2] \frac{B_{\text{eff}}^2 [\text{T}^2]}{2} L_w [\text{m}] I_e [\text{A}]. \quad (5)$$

The critical energy  $E_c$  of a synchrotron radiation source is normally defined as the photon energy which divides the radiation spectrum into two regions with equal power. For the computations which follow, the standard expression for the critical energy [10] has been used:

$$E_c [\text{keV}] = 0.665 \times E_c^2 [\text{GeV}^2] B_{\max} [\text{T}] = 7.0 \text{ keV}. \quad (6)$$

A “Mathematica<sup>®</sup>” program which implements Tatchyn’s expressions is included in Appendix B.

The preliminary analysis of the MS-wiggler considered a field profile symmetric about  $z = 0$  and which contained only the first two terms in the series for  $B(z)$ :

$$B(z) = \frac{B_{\max}}{(1-\eta)} \left[ \sin \left( \frac{2\pi z}{\lambda_w} \right) + \eta \sin \left( \frac{6\pi z}{\lambda_w} \right) \right], \quad (7)$$

where  $\eta = B_1/B_0$  is the Fourier amplitude ratio. Tatchyn’s treatment is applicable when  $B(z)$  has a single local maximum and minimum within each period, implying  $-1/3 < \eta < 1/9$ .

The length of the available straight section dictated a maximum wiggler length  $L_w$  of 2 m. To maximize  $B_{\max}$ , it was decided to use a wiggler magnetic gap  $w = 8$  mm and a realization of the Halbach magnet array [6] with NdFe:B magnetic blocks and FeCo (“Permendur<sup>®</sup>”) pole pieces. For compatibility with the overall beamline length (see Section 6.5) and the dimensions of practical optical elements, the horizontal divergence accepted by the beamline was specified to be 2.5 mrad. The principal wiggler parameters then to be optimized were the wiggler period  $\lambda_w$  and the field profile parameter  $\eta$ , the latter effectively determined by the length ratio between the magnetic blocks and the pole pieces.

Halbach has presented empirical formulae for the maximum field obtainable with different magnetic materials [6]. The expression corresponding to NdFe:B, is [11]

$$B_{\max} [\text{T}] = 3.27 \exp \left[ -\frac{w}{\lambda_w} \left( 5.08 - 1.54 \frac{w}{\lambda_w} \right) \right]. \quad (8)$$

A calculation was performed, using Tatchyn’s algorithms, of the spectral flux density (photons/s/

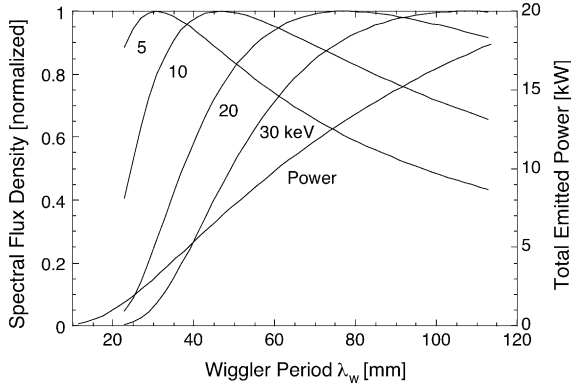


Fig. 2. Calculated spectral flux density (normalized), at four pertinent photon energies, and the total power emitted by the wiggler, as a function of the wiggler period  $\lambda_w$ . The wiggler gap is  $w = 8$  mm, the wiggler length is  $L_w = 2$  m, and the profile parameter is  $\eta = 0$ . A good compromise value for  $\lambda_w$  is 60.5 mm.

0.1% bandwidth divided by the FWHM horizontal profile width) at relevant photon energies and of the total power emitted by the wiggler, as a function of the wiggler period  $\lambda_w$  (see Fig. 2). Here it was assumed that  $\eta = 0$ , i.e.,  $B(z)$  has a sinusoidal field profile. These calculations indicate that a reasonable value for  $\lambda_w$  is 60.5 mm. Hence the MS-wiggler is known as “W61”.

The optimum Fourier amplitude ratio  $\eta$  was determined with the aid of numerical calculations of the field profile for varying ratio of magnet block to pole piece length. The computed value of  $B_{\max}$  as a function of the resulting  $\eta$ , for a period of 60.5 mm, has a behavior which can be approximated over the range  $-0.22 < \eta < 0.16$  with the polynomial:

$$B_{\max}[T] \approx 1.44 - 2.05\eta + 1.70\eta^2 - 69.1\eta^3 - 78.2\eta^4 + 1530\eta^5. \quad (9)$$

The maximum value of  $B_{\max} = 1.90$  T, at  $\eta = -0.176$ , exceeds the value of 1.71 T predicted by Eq. (8). A computation with the Tatchyn algorithms of the spectral flux within the horizontal divergence accepted by the beamline (2.5 mrad) confirms that this value also represents an optimum over the entire photon energy range of

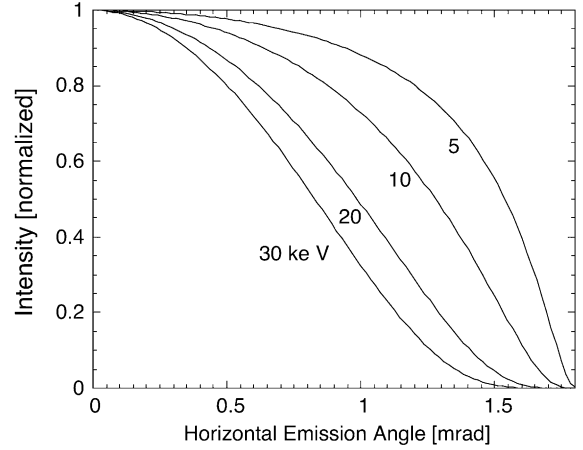


Fig. 3. The computed horizontal emission profiles of the W61 wiggler as a function of photon energy. The fixed front-end aperture of the beamline accepts a full horizontal width of 2.5 mrad.

interest. Final numerical optimization gave  $\eta = -0.163$ , implying a pronounced “sawtooth” character of the field profile  $B(z)$ .

The divergence of the wiggler radiation was computed as follows: In the vertical direction, it was assumed that the radiation has a Gaussian profile, with a FWHM given by [10]

$$\Delta\theta_{\text{FWHM}}[\text{mrad}] = \sqrt{8 \ln 2} \times 1000 \times 0.58 \times \frac{1}{\gamma} \times \sqrt{\frac{E_c}{E}} \quad (10)$$

which (with  $E_c = 7.0$  keV) yields values of 0.34 and 0.12 mrad at  $E = 5$  and 40 keV, respectively. Consequently, the vertical divergence accepted by the beamline was chosen to be 0.23 mrad.

For the horizontal plane, Tatchyn’s formulae (Appendix B) for the spectral flux into a horizontal aperture were differentiated to obtain the energy-dependent horizontal emission profiles (see Fig. 3). Tatchyn’s analysis yields a spectral flux into our  $0.23 \times 2.5$  mrad<sup>2</sup> aperture which agrees to within a factor of two with a complete numerical calculation, using the program “SRW” [12]. The final design optimization and construction of the wiggler were performed by the company Danfysik, Jyllinge, Denmark.

#### 4. The front-end safety system

The functions of the beamline “front-end” (components in the ring tunnel, after the wiggler) are: (a) to monitor the vertical position of the photon beam, (b) to define the angular acceptance, (c) to block, when required, the X-ray and Bremsstrahlung radiation, for access to the optics hutch, (d) to filter out the soft radiation and (e) to isolate the beamline vacuum from the storage-ring vacuum.

Two staggered-blade X-ray beam-position monitors (XBPMs) [13] are included in the front-end, at 8.58 and 11.66 m from the source. The photocurrents in the blades, up to 0.1 mA, permit an intensity independent, vertical position determination over a region of 0.5 mm and with an accuracy of 1  $\mu\text{m}$ . The fixed aperture (at 9.67 m), is a rectangular funnel made of four inclined, water-cooled copper plates, with an opening of  $2.2 \times 24.2 \text{ mm}^2$ , which limits the angular acceptance to  $0.23 (v) \times 2.5 (h) \text{ mrad}^2$ . A shutter (at 10.22 m) closes the X-ray beam, and a Bremsstrahlung blocker (at 11.17 m) stops the (up to 2.4 GeV) gamma rays. The photon shutter is an angled, water-cooled copper head which can be pneumatically inserted, and the Bremsstrahlung blocker is an uncooled tungsten cylinder, 55 mm in

diameter and 180 mm long, which is likewise pneumatically inserted, after a short delay.

A particularly important component of the beamline is the filter (at 12.14 m) to remove the soft X-rays, which would otherwise destroy the Be-vacuum window. The filter material must be low- $Z$  and tolerate a high heat load. The beam size at the filter is  $3 \times 30 \text{ mm}^2$ , and it was originally planned to use a 1 mm thick CVD-diamond plate. However, tests in which 1 kW from a  $\text{CO}_2$ -laser beam of this size was absorbed in a Cr-coated diamond plate in a water-cooled Cu-frame resulted in fracturing. It was then decided to use a piece of high-temperature, glassy-carbon (“Sigradur G”<sup>®</sup>, atomic density  $\rho_a = 0.118 \text{ mol/cm}^3$  [14]), which is continually rotated to distribute the heat. The design chosen (see Fig. 4) is based on a Sigradur cup, 70 mm in diameter and 82 mm high, with a wall thickness of 1 mm. A commercially available cup underwent final on-site machining using electro-erosion. The cup is mounted on a horizontal spindle and enclosed from within and without by a blackened, two-piece, water-cooled copper housing. The X-ray beam traverses the cup wall twice, perpendicular to the cup axis. The cup is rotated at 5 Hz, and the rotation speed and motor drive current are continuously monitored, along with the temperature at three

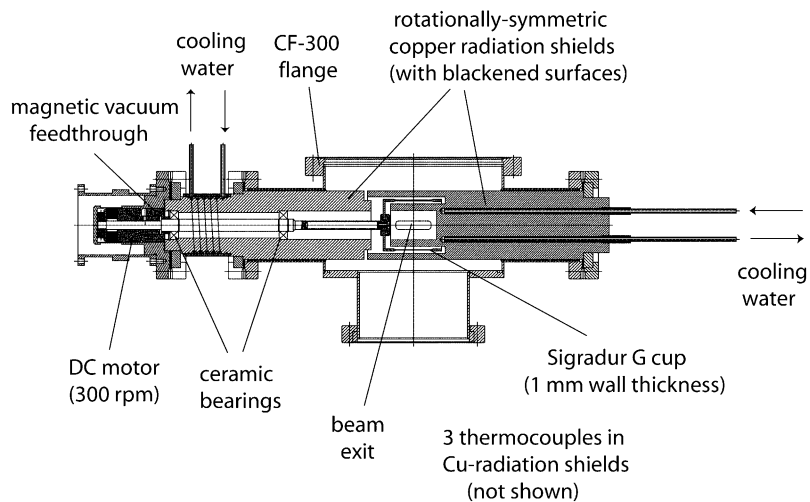


Fig. 4. A schematic plan of the rotating carbon filter.

points in the copper housing. A weak point of this filter design is the spindle bearings, which must operate continuously in ultra-high vacuum. Silver-coated bearings were first used, but they failed after 2700 h. Ceramic bearings were then installed and have been in operation since March 2002. An improved design would use magnetic bearings.

For optional further reduction of the beam divergence, two cooled, crossed, slit-pairs are situated 13 m from the source. The final front-end component is a double Be-vacuum-window (at the beginning of the optics hutch, 15.43 m from the source). In the double window design [15], a polished, thick (500  $\mu\text{m}$ ), soldered, upstream window provides UHV-isolation, and an unpolished, thin (50  $\mu\text{m}$ ), clamped, downstream window protects against a possible pressure surge. To monitor the integrity of the rotating carbon filter, a photodiode measures the amount of reflected UV-radiation from the upstream window. The maximum absorbed heat-loads in the front-end components are presented in Table 5.

Table 5  
Maximum heat loads (at 300 mA)

Total wiggler emission	5.7 kW
Passed by fixed aperture	2.9 kW
Absorbed in C-filter	1.6 kW
Absorbed in Be-window	24 W
Transmitted by front-end	1.2 kW
Absorbed in mirror 1 (at 5–10 keV setting)	0.92 kW
Absorbed in crystal 1 (at 18.5 keV setting)	0.56 kW
Transmitted by optics (at 14 keV)	90 mW

## 5. The X-ray optics

### 5.1. General considerations

The X-ray optical system of the beamline performs four tasks: (a) photon-energy selection using a fixed-exit double-crystal monochromator (DCM), (b) optimization of the energy resolution with a collimating mirror (M1) upstream of the DCM, (c) vertical focusing at variable experimental positions with a focusing mirror (M2), and (d) horizontal focusing by a sagittally bent second DCM-crystal (X2). These tasks are performed by the mirror–DCM–mirror system, shown schematically in Fig. 5. Further advantages of this configuration are that M1 absorbs a significant amount of heat which would otherwise strike the first DCM crystal (X1), and that, by setting the M1 angle just below the critical angle, higher harmonics transmitted by the DCM are suppressed. The DCM-crystals X1 and X2 are mounted on a common rotation stage, with the rotation axis coincident with the diffracting surface of X1. A change in photon energy involves a rotation about this axis, and, in order to guarantee fixed-exit conditions, X2 can be moved with two orthogonal translation stages. Fine-tuning of the crystal parallelism is provided by rocking X2. Lateral beam steering is accomplished by rolling X2, and an axial rotation of the (asymmetric) focused beam is produced by yawing X2.

The optical system has several modes of operation. The normal mode is “collimated and focused monochromatic” beam, with mirrors and crystals inserted. Usually, the (1 1 1)-reflections of the Si DCM-crystals are used, yielding a

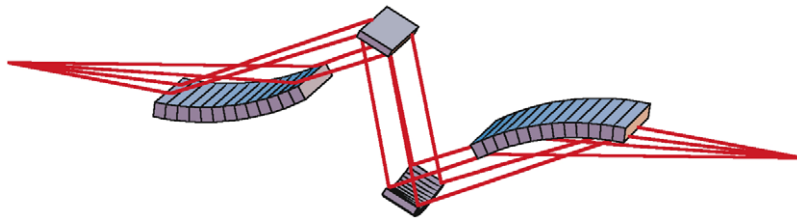


Fig. 5. A schematic view of the beamline optics. The source is at the left, and the experimental station is at the right. The components, from left to right, are: cylindrical vertically collimating mirror (M1), flat first crystal (X1), sagittally focusing second crystal (X2), and cylindrical vertically focusing mirror (M2).

theoretical energy resolution  $\Delta E/E = 1.39 \times 10^{-4}$ . For photon energies above 10 keV it is also possible to use the (333)-reflections, reducing  $\Delta E/E$  to  $9.5 \times 10^{-6}$ . At the cost of energy resolution and vertical focusing, the two mirrors can be removed from the beam-path, producing a “mirrorless monochromatic” beam, without vertical collimation or focusing, but also without aberrations from mirror slope-error. Finally, a “pink beam” mode is available, for which the monochromator crystals are removed from the beam-path and M2 is raised high enough to reflect the polychromatic beam from M1. Since the polychromatic beam is extremely intense, it is restricted in width by a narrow slot in the fixed Bremsstrahlung blocker (see below), limiting the maximum transmitted power to 200 W. Pink beam is useful when surveying the position of X1 with synchrotron radiation. Only the first mode, “collimated and focused monochromatic” with (111)-reflections, will be discussed here.

The chosen optical design spans the photon-energy range from the point at which the carbon filter and Be-windows begin to transmit (5 keV) to the end of the usable wiggler spectrum (40 keV). Alternative designs use interchangeable crystals and/or mirrors with multiple coating stripes, in order to tailor the resolution and flux in different energy regions. However, considerations of crystal-holder weight and a high mirror heat-load, requiring a symmetric distribution, dictated our choice of a single set of crystals and a single mirror coating. The silicon (111)-reflection is a standard choice for the monochromator, representing a compromise between resolution and transmission. The choice of Rh-coated mirrors yields a large critical angle over the entire energy range, with a single disturbing absorption edge at 23.22 keV.

Extensive simulations of the motions of the mirrors-DCM system were made. One issue was the “beam-offset”—the net vertical displacement of the radiation after traversing the optical system. To limit unwanted background, the beam-offset must be larger than the size of the cone of Bremsstrahlung radiation. But a large beam-offset lengthens the axial X2-movement, hence enlarging the DCM-vacuum-chamber. Simulations of gas Bremsstrahlung [16] indicated a minimum beam-

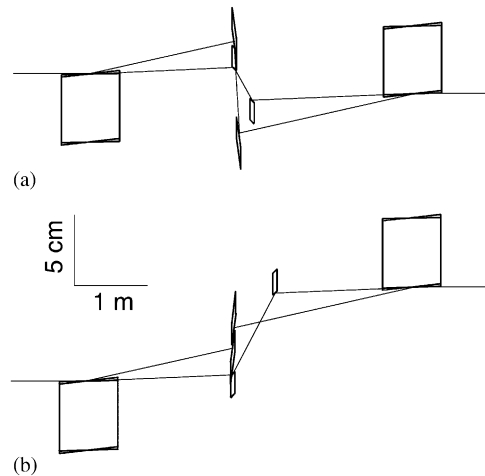


Fig. 6. A comparison of mirror and crystal placement for the cases of (a) “up-down-up-down” and (b) “up-up-down-down” geometries. In each case, the photon beam enters from the left, strikes the first mirror, the first crystal, the second crystal and the second mirror. Two situations are drawn for each case: 5 and 40 keV photon energy. Note the large beam offset required in case (b), in order to avoid shadowing of the second crystal at low energy, and the long second crystal translation (large DCM vacuum tank) which results.

offset of 15 mm, corresponding to an angular offset at the Bremsstrahlung blocker (see below) of  $3.5/\gamma$ . Another issue was the sense of successive mirror and crystal reflections. The liquid-metal cooling of M1 (see below) dictated an upward reflection for this mirror. The choice for X1 between upward- and downward reflection was decided by the excessive beam-offset required in the former case to avoid a shadowing of X1 by X2 at low photon energies (see Fig. 6). Finally, it was found that the axial X2-movement could be further reduced by varying the mirror angle with each change in photon energy. For operation at 5 keV, this requires raising the DCM-vacuum vessel 23 mm above the synchrotron plane. As will be described below, the possibility of independently setting the photon energy and the mirror angle allows the realization of useful diagnostic methods.

## 5.2. The optical components

The optical system of the MS beamline has approximately a “1:1 configuration”, implying

roughly equal source–optics and optics–experiment distances. This is the optimal situation for approximating ideal elliptical focusing surfaces by cylindrical ones. To keep the curvature of the elements to a minimum, to allow space for three sequential experimental stations and to minimize the angular divergence in diffraction experiments, the overall length of the beamline was set to the maximum allowable by the SLS building: approximately 40 m (see Section 6.5). With the  $0.23 \times 2.5 \text{ mrad}^2$  angular acceptance, the resulting beam size at the optics is approximately  $5 \times 50 \text{ mm}^2$ . Together with the mirror and crystal angles, this dictates the size of the optical elements.

### 5.2.1. The mirrors

The collimating (M1) and focusing (M2) mirrors are virtually identical in mechanical design and optical quality; the principal difference is that M1 reflects upward and M2 downward. The mirrors were designed and manufactured by SESO, Aix en Provence, France. They are made of crystalline Si and coated with 5 nm Cr plus 60 nm Rh. The overall dimensions (length, width, thickness) of M1 and M2 are (1010, 95, 65) and (950, 85, 65) mm, respectively, and the optically usable area for both mirrors is  $800 \times 55 \text{ mm}^2$ . During monochromatic operation, the thermal load on M1 (see below) is much larger than that on M2, but in the pink-beam mode, up to 200 W can be absorbed in M2. The mirrors are cooled via machined grooves in the upper surface, parallel to the long axis, which contain liquid Ga–In–Sn–eutectic and into which Ni-plated, water-cooled copper plates are immersed. Since the heat in M2 must traverse the mirror thickness, the maximum thermal distortions are comparable in the two mirrors.

The quality of the mirrors has been optically checked by the manufacturer. Averaged over the usable area, the measured rms roughness and rms slope error of M1 are 0.27 nm and  $0.75 \mu\text{rad}$ , respectively, and the corresponding values for M2 are 0.25 nm and  $1.38 \mu\text{rad}$ . Dual counterweight arrangements minimize gravity sag. Using motor-driven mechanical clamps, the mirrors can be cylindrically bent from their unstrained, slightly convex shape to a minimum radius of curvature of 5 km. Each mirror bender is rigidly attached to a

metal plate outside of the vacuum vessel, which is in turn supported by three stepping-motor jacks, for setting the height, pitch and roll.

The critical angle  $\alpha_c$  for total X-ray reflection from a metal surface is proportional to the square-root of the electron density of the metal. Because of columnar growth and other defects, the density of a thin evaporated metal film can lie substantially below the bulk value. To measure the density of our Rh-mirror coatings, the reflectivity of the M1–M2 pair, equal to the square of the reflectivity of a single mirror, was measured as a function of photon energy and mirror angle. In Fig. 7, the results (dots) are compared with the Fresnel theory [17], assuming the bulk Rh-density (solid curves) and a reduced density (dashed curves). The observed 30% decrease in Rh-density is, according to the manufacturer, at the high end of the expected range, and can be reduced by a treatment with ion-implantation. During beamline operation, the two mirror angles are set equal (to guarantee a horizontal beam) and to approximately 85% of the measured critical angle. For energy settings below 10 keV, the mirror angles are fixed to 85% of the 10 keV critical angle.

The collimating mirror M1 has the task of producing a parallel beam in the vertical direction prior to entry into the DCM, in order to optimize the energy resolution  $\Delta E/E$ . From the Coddington equations (Appendix C, Eq. (C.2)),

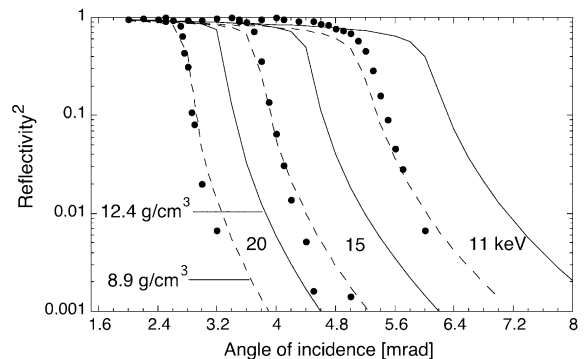


Fig. 7. The predicted (solid curves) and measured (dots) reflectivity of the two-mirror system, as a function of the angle of incidence and of the photon energy. The measurements demonstrate that the effective density of the Rh-coating is  $8.9 \text{ g/cm}^3$  (dashed curves) instead of the bulk value of  $12.4 \text{ g/cm}^3$ .

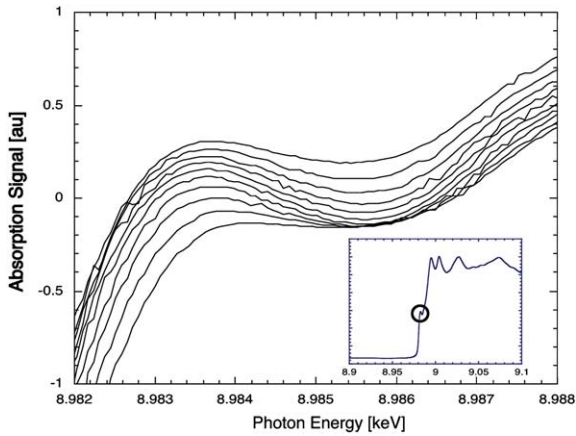


Fig. 8. The pre-edge absorption feature of a 7.5  $\mu\text{m}$  copper foil, measured as a function of the bending of the collimating mirror. The beam intensity was reduced, such that thermal deformation of the optics could be neglected. In the case shown, the mirror angles were 4 mrad, and the bending radius of the collimating mirror was varied from 5.6 to 8.8 km. The inset shows the K-absorption edge of copper on a coarser energy scale, with the pre-edge feature circled.

the required radius of mirror curvature  $R_{\text{meridional}}$  ( $q = \infty$ ), is given by

$$R = \frac{2L}{\sin \theta_M} \quad (11)$$

where  $L$  is the source–M1 distance, and  $\theta_M$  is the mirror angle. The mirror curvature at various mirror angles has been optimized empirically by making use of the visibility of the narrow pre-K-edge absorption feature in metallic copper (see Fig. 8). In this way, the M1 curvature was calibrated as a function of the travel of the bending actuator. The valley and peak energies of the pre-edge are separated by 2.1 eV, or  $2.3 \times 10^{-4}$  of the edge energy. From the visibility of this feature, we conclude that  $\Delta E/E$  is better than or of the order of  $10^{-4}$ , as expected for the Si (1 1 1) DCM crystals. Under collimating conditions for M1, the optimal radius of curvature of M2, for focusing at an experimental station at a distance  $L$ , is also given by Eq. (11). (If M1 is not collimating, a more complex formula, given in Appendix C, is required.) A calibration of the M2 curvature could thus be performed by minimizing the vertical size of the focus spot at different

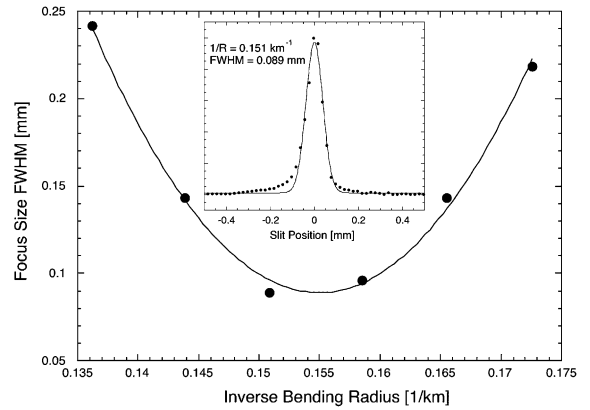


Fig. 9. The vertical size of the pink beam, measured by scanning a slit at a distance from the source of 36.1 m, as a function of the bending of the focusing mirror. The beam intensity was reduced, such that thermal deformation of the optics could be neglected. For this case, the mirror angles were set to 4 mrad, and the first mirror was bent to the optimum collimating curvature. The inset shows a differentiated slit scan for a mirror curvature of  $0.151 \text{ km}^{-1}$ .

mirror angles (see Fig. 9). The focus size was measured by scanning a slit in front of a detector at a distance of 34.83 m from the source. During these measurements, a reduced-intensity pink beam was used, and the (already calibrated) curvature of M1 was accounted for. The resulting (linear) dependences of the M1 and M2 mirror curvatures ( $1/R$ ) on the actuator travels showed similar slopes to those supplied by the manufacturer, but with significant offsets, indicating a loosening of the actuators since the factory tests.

### 5.2.2. The monochromator

The DCM-crystals are responsible for selection of the photon energy. The use of two crystals in a non-dispersive arrangement (“zig-zag” reflection path) provides a fixed exit from the DCM and a high integrated transmission, but requires the use of an upstream collimating mirror for optimal energy resolution. The MS-beamline uses two well-established crystal designs: the “Hasylab-TORII” design [18] for X1 and the “ESRF flexure-hinge-bender” design [19] for X2. Both crystals are housed in a large, cylindrical monochromator

vacuum tank, which provides the crystal motions already noted, along with the crystal cooling. The entire monochromator assembly, excluding the crystal systems, was built by Kohzu, Tokyo, Japan.

The TORII system [18] is based on a crystal ( $90 \times 90 \text{ mm}^2$ ) in the shape of an (inverted) table. The beam strikes the crystal surface from below, while a water-cooled, Ni-plated copper block, situated between the table legs and in contact via a Ga–In–Sn eutectic film, removes the absorbed heat. The thermal load produces a convex curvature of the crystal, which is dynamically corrected by pressing the two leaves of the table, at the front and back ends of the unit. This pressure is applied via the thermal expansion of electrically heated copper rods, and the applied force is monitored via strain gauges mounted on weak links connected to the table leaves. A feedback system adjusts the rod-heating to maintain a preset strain. Finite-element modelling of the TORII system, based on the Tagaki–Taupin equations [20] predicts a 40% loss of beam intensity at an absorbed heat load of 1 kW, even with optimal compensation. The predicted heat-loads in M1 and X1, at 300 mA electron current, are shown as a function of photon energy setting in Fig. 10. Rocking curves of X2, without sagittal focusing, are shown in Fig. 11, at different settings of the X1 TORII strain. To minimize vibrations from pressure fluctuations, cooling of the TORII system is performed using a dedicated cooling circuit, in which the water is pulled with a pump through the crystal system from a reservoir. The pressure before the pump must be adjusted to avoid boiling.

The second crystal, X2, provides sagittal (horizontal) focusing of the beam (see Appendix C). To minimize anticlastic bending, the ESRF flexure–hinge–bender design [19] uses a Si (111) crystal ( $120 \times 95 \times 10.7 \text{ mm}^3$ ) into which grooves (1.4 mm period, 1 mm wide, 8.2 mm deep) are cut. The resulting  $400 \mu\text{m}$  wide ribs serve to stiffen the crystal in the direction perpendicular to the bending. The crystal is soldered into edge clamps, which in turn are mounted on two flexure–hinge assemblies, whose function is to maintain the center of the crystal at a constant

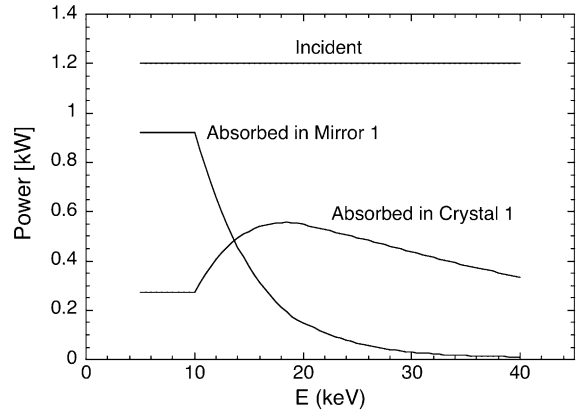


Fig. 10. Predicted heatloads in the beamline optics, for an electron current of 300 mA and a wiggler gap of 8 mm, as a function of the photon energy setting.

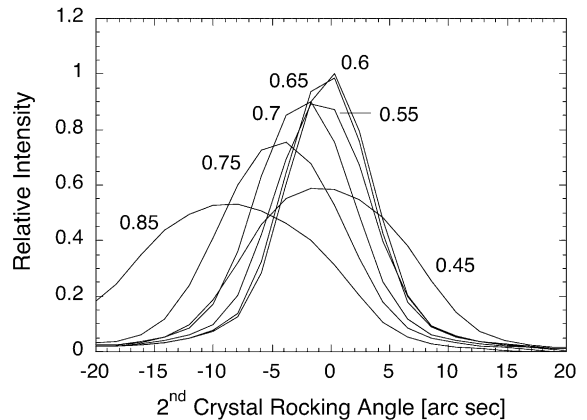


Fig. 11. Second-crystal rocking curves, without sagittal focusing, as a function of the TORII strain setting of the DCM crystal X1. The numbers give the controller signal in volts. The conditions are: 330 mA electron current, 8 mm wiggler gap and 10 keV photon energy, and the minimum rocking curve width is 9.3 arcsec. The shift in optimum rocking angle with strain setting indicates a slight misalignment.

height as the curvature is varied. Two step-motors with gearboxes move actuator bars, producing an X2 radius of curvature as small as 1 m. In general, identical displacements of the two actuators are used. Although the flux impinging on X2 only represents milliwatts of power, flexible copper bands have been included from the

clamps to the water-cooled base, in order to remove radiative heat generated by X1. A second closed-circuit cooling system, identical to that serving X1, is used to cool X2 and several radiation shields inside the DCM vacuum tank. A potential problem with this crystal mounting system is a possible crystal twist introduced during the soldering process. During mounting, this twist was monitored via the observation of optical interference fringes, using an optical flat placed on the crystal surface.

### 5.2.3. Auxiliary components of the optical system

In addition to the mirrors and DCM, the present optical system includes the auxiliary components described below.

A water-cooled “fast absorber” can be pneumatically inserted (at 16.10 m) into the beam at the beginning of the optics hutch within a fraction of a second, in order to quickly react to an alarm from the equipment protection system. In a controlled experiment, the cooling water to the absorber was switched off, and its temperature rise was measured upon insertion into the beam. In this way, the predicted wiggler flux was confirmed in a calorimetric measurement. The fast absorber will soon be modified to include a pinhole array, to allow downstream imaging of optical aberrations.

Two water-cooled filters can be pneumatically inserted into the white beam (at 16.23 m) in order to reduce intensity for test purposes or during photon-energy changes. The “thin” filter consists of 5 mm of pyrolytic graphite, and the “thick” filter consists of 15 mm of graphite plus 75  $\mu\text{m}$  of molybdenum.

Between the first mirror and the DCM (at 18.66 m), a 100  $\mu\text{m}$  tungsten wire can be vertically scanned through the beam. The resulting photoelectron current is read-out with a nanoampere meter, allowing a measurement of the beam’s vertical position and profile.

The M1-DCM combination diverts the monochromatic beam below the synchrotron plane. Following the DCM (at 20.42 m), a fixed Bremsstrahlung blocker is situated, consisting of a cooled copper plate followed by a massive block (65 mm thick) of tungsten. While the blocker interrupts any Bremsstrahlung in the synchrotron

plane (nominal height: 1.4 m from the floor), a channel below this height allows the monochromatic beam to pass. In addition, a narrow slit above the nominal height allows passage of the polychromatic pink beam.

Following M2, there are two Kapton<sup>®</sup> windows, forming a 30 cm air gap. Into this gap, objects can be inserted such as a diffractive focusing element for imaging the wiggler source or a rotating paper wheel for improving the quality of tomographic images by washing out profile inhomogeneities arising from mirror slope errors (see Section 6.4). For high-intensity pink beam operation or to avoid absorption by air at low photon energies, the gap can be closed and the windows removed.

At the end of the optics hutch, a cooled “first station shutter” (at 23.77 m) can be pneumatically inserted into the beam, to allow access to the experimental hutches without causing the X-ray optics to cool down. An uncooled “second station shutter” (at 37.92 m) allows access to the second experimental hutch during experiments in the first hutch.

Besides the front-end slits, there are two additional sets of horizontal and vertical slits along the beamline: a cooled set at the beginning of the first experimental hutch (at 30.62 m) and an uncooled set at the beginning of the second experimental hutch (at 38.60 m). These are useful for limiting the divergence and reducing background. Additional fine slits are included in each experimental station.

Two remotely insertable fluorescent screens, with optical windows and video cameras, are installed behind the Bremsstrahlung blocker in the optics hutch and behind the uncooled slits in the second experimental hutch. The screens provide a quick check of the beam intensity and profile during setup.

## 6. Optical performance of the beamline

### 6.1. Spectral flux

A prediction of the spectral flux produced by the beamline is a somewhat involved process, includ-

ing consideration of: (a) the spectral wiggler emission into the beam-defining aperture, (b) the absorption by the rotating carbon filter and the Be-windows, (c) the beam footprint at and the reflectivity of the mirrors, (d) the bandpass of the DCM crystals and (e) the absorption by other beamline windows and air paths. A documented “Mathematica<sup>®</sup>” program which performs this calculation is included in Appendix B.

The energy-dependent DCM-bandpass requires special mention. If  $R(E)$  is the energy-dependent crystal reflectivity and  $g(E)$  is the spectral-flux (photons/s/0.1% bandwidth) incident on the DCM, the transmitted flux  $F$  (photons/s) after two crystal reflections is given by

$$F = \int_0^\infty R^2(E') \frac{1000}{E'} g(E') dE' \approx 1000g(E) \frac{\Delta E}{E} \quad (12)$$

where the monochromator bandpass (energy resolution)  $\Delta E/E$  is given by

$$\begin{aligned} \frac{\Delta E}{E} &= \int_0^\infty R^2(E') \frac{dE'}{E'} = \int_0^\infty R^2(\theta) \left| \frac{\partial E}{\partial \theta} \right| \frac{d\theta}{E(\theta)} \\ &= \int_0^\infty R^2(\theta) \cot \theta d\theta \approx \cot \bar{\theta} \Delta\theta. \end{aligned} \quad (13)$$

Here, the energy-angle relation (Planck and Bragg) has been used:

$$E(\theta) = hv = \frac{hc}{\lambda} = \frac{hc}{2d \sin \theta} \approx \frac{1.977 \text{ keV}}{\sin \theta} \quad (14)$$

where  $d = 3.136 \text{ \AA}$  is the Si (1 1 1) lattice spacing. The Si (1 1 1) Bragg reflectivity  $R(\theta)$  is calculated with the dynamic theory of crystal diffraction [21]. To first approximation,  $R(\theta)$  is unity within an angular region of width  $\Delta\theta$  (the “Darwin width”) around the Bragg angle and zero otherwise, hence the right-hand approximate equality in Eq. (13). Ignoring absorption in the silicon,  $\Delta E/E$  is a constant equal to 0.000139, and including absorption, it can be approximated in the range 5–40 keV by the formula:

$$\left. \frac{\Delta E}{E} \right|_{(111)} \approx (1.396 - 16.22E[\text{keV}]^{-1.963}) \times 10^{-4}. \quad (15)$$

This is the expression used in the program in Appendix B.

Three measurements of the spectral flux have been performed, two using an ionization chamber as a detector, with flowing  $\text{N}_2$  (for  $E < 20 \text{ keV}$ ) or Ar ( $E > 20 \text{ keV}$ ), and the third using a calorimeter ( $E < 20 \text{ keV}$ ). In all three cases, the focused intensity at 36.1 m from the source was measured as a function of the photon-energy. A commercial ionization chamber with 33 mm electrode length was used (S-1329A, Oken Corp., Saitama, Japan), with an applied voltage of 1000 V ( $\text{N}_2$ ) or 1500 V (Ar). In order to convert the measured current into a photon flux [22], the energy-dependent absorption of 33 mm of the gas was considered, along with an energy required per electron–ion pair of 36 eV ( $\text{N}_2$ ) or 24.4 eV (Ar). The calorimetric measurement made use of a commercial laser power-meter. In this calibrated, windowless device, the radiation impinges on a blackened disk of aluminum, and a thermal gradient is measured near the edge using thermocouples. At high photon energies, a correction for the absorption in the 400  $\mu\text{m}$  thick disk is required. A comparison between the predicted and measured spectral flux is shown in Fig. 12. For the predicted flux curve, the absorption produced by a total of 51 cm of air path and 875  $\mu\text{m}$  of Kapton<sup>®</sup> windows has been included. The discrepancy between prediction and measurement is attributed to imperfect compensation of the thermal load in the first DCM-crystal (see Section 5.2.2) and to a reduction in DCM transmission due to distortions in the second crystal from the sagittal focusing [23].

In order to obtain the power in the beam, one integrates the spectral flux density times the photon energy:

$$P = \int_0^\infty \frac{1000g(E')}{E'} E' dE'. \quad (16)$$

For a photon-energy given in keV, the power in kW is obtained by

$$P[\text{kW}] = 1000e \int_0^\infty g(E') dE' \quad (17)$$

where  $e = 1.602 \times 10^{-19} \text{ C}$  is the electron charge in Coulombs. This is the expression used in the program in Appendix B to compute the heat-load

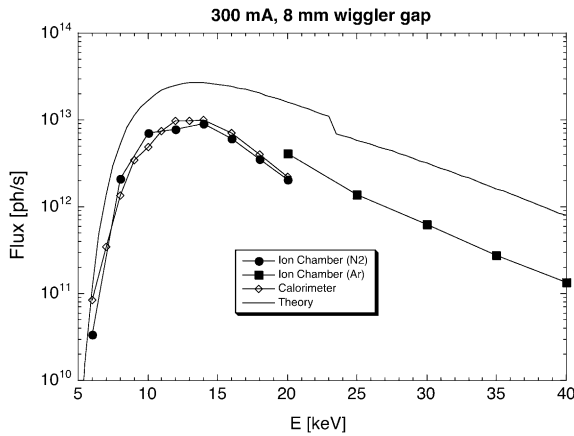


Fig. 12. The predicted flux at 300mA electron current and 8 mm wiggler gap, and flux measurements using an ionization chamber with N<sub>2</sub> and Ar and a laser power calorimeter.

values in Table 5 and in Fig. 10. It should be noted that the heat-loads in the C-filter and Be-windows are in principle sensitive to the optical properties of these materials below the 5 keV minimum energy of the beamline. For the sake of simplicity, however, their low-energy absorption-edge structure was neglected (see Appendix A).

### 6.2. Harmonic contamination

Besides the (1 1 1) fundamental, the DCM also transmits radiation at higher harmonics, due to the (2 2 2) and (3 3 3) Bragg reflections of silicon. These harmonics are suppressed by the lower wiggler flux at high energy, the low mirror reflectivity above the critical energy and the low Si scattering factors; the (2 2 2)-reflection is only allowed due to the asphericity of the atomic electron distribution and to anharmonic lattice vibrations.

Predictions of the harmonic flux contaminations are presented in Fig. 13. These are based on numerical calculations of the DCM-bandpass for the (2 2 2)-reflection at twice the fundamental energy  $E$  and for the (3 3 3)-reflection at three times  $E$ . A scattering factor for the (2 2 2) reflection of 0.18 electrons for each of the 8 atoms per conventional unit cell was assumed [24]. Using dynamic diffraction theory (as outlined in the previous Section) and accounting for absorption,

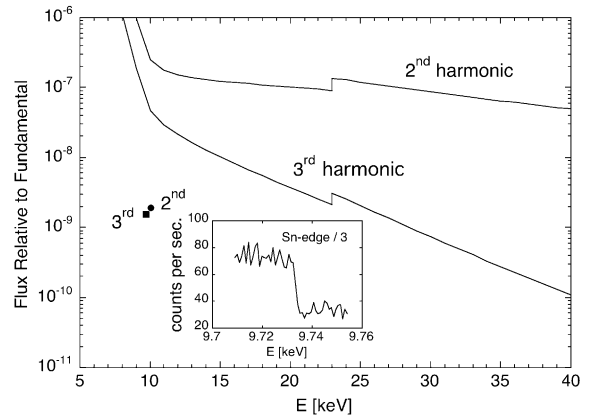


Fig. 13. The predicted harmonic contamination at twice and three times the fundamental beamline energy  $E$ , from the (2 2 2) and (3 3 3) Si reflections in the monochromator. The harmonics are suppressed by the mirror reflections. The experimental points at 10 keV were measured as described in the text. The inset shows the observed third-harmonic absorption at the Sn K-edge (29.20 keV).

the following approximate expressions for the bandpasses are obtained:

$$\frac{\Delta E}{E} \Big|_{(2\ 2\ 2)} \approx (8.83 - 9.19E[\text{keV}]^{-0.0374}) \times 10^{-6},$$

$$\frac{\Delta E}{E} \Big|_{(3\ 3\ 3)} \approx (9.51 - 28.13E[\text{keV}]^{-2.038}) \times 10^{-6}.$$
(18)

Also shown in Fig. 13 are measurements, at a beamline setting of  $E = 10$  keV, of the second- and third-harmonic intensities, at 20 and 30 keV, respectively. This was accomplished by introducing attenuation foils into the beam, to reduce the fundamental component, along with an absorber foil with an absorption edge near the desired energy, the thickness of which is optimized for maximum contrast [25]. For this purpose, 15  $\mu\text{m}$  of Mo (K-edge at 20.00 keV) and 58  $\mu\text{m}$  of Sn (K-edge at 29.20 keV) were used. A scan of the fundamental energy around 10 keV produced a step in the counting rate in a scintillator detector (with the discriminator threshold adjusted for sensitivity beyond the third harmonic), allowing a determination of the harmonic flux. The inset in the figure shows the counting rate per second, after passing 3 mm of Al plus 58  $\mu\text{m}$  of Sn, as a function

of the fundamental beamline energy. Note the step at 9.733 keV, which is 1/3 of the Sn K-edge energy. The 10 keV experimental results are remarkable in two respects: A larger difference between the second- and third-harmonic fluxes was expected, and both fluxes are much lower than predicted. Although we have no definitive explanation for these deviations, possible causes could be related to interference of the penetrating harmonic radiation due to reflection from the Si mirror substrate or to a depth-dependent micro-roughness associated with the porous nature of the Rh-coating. In addition, the narrow rocking curve widths at high energy make the harmonics more sensitive to crystal deformations.

### 6.3. Focus spot size

A prediction of the focus spot size [17] should consider the finite source size, the mirror-related effects of spherical aberration, coma and slope-error and sagittal-focusing aberrations by the second DCM-crystal [23]. The approximately 1:1 optics of the MS-beamline and the fact that the lengths of the mirrors are a small fraction of their focal lengths allow one to neglect the effects of spherical aberration and coma. As will be seen in the following subsection, the effective FWHM vertical source size for the beamline, for intermediate photon energies, is  $\Delta s = 75 \mu\text{m}$ . The source-size contribution to the vertical focus size is thus  $\Delta y_{\text{source}} = |M\Delta s|$ , where  $M$  is the vertical magnification of the beamline. For a single mirror with an rms slope-error  $\delta\theta_M$  and a mirror-focus distance  $q_M$ , the FWHM vertical spot-size is given by [17]

$$\Delta y_{\text{slope}} = 2\sqrt{8 \ln 2} \delta\theta_M q_M. \quad (19)$$

Since the influence of slope-error on our *two*-mirror optics is difficult to evaluate analytically, we make use of a numerical simulation of its contribution  $\Delta y_{\text{slope}}$  to the vertical focus using the program “Phase” [26], where  $\delta\theta_{M1} = 0.75 \mu\text{rad}$  and  $\delta\theta_{M2} = 1.38 \mu\text{rad}$ , the average rms slope-errors measured by the manufacturer over the active areas of M1 and M2, respectively, are taken as input.

Two situations have been investigated: (a) The vertically focused pink-beam measurement

presented in Fig. 9, performed near the PDiff-station, gave a FWHM focus size  $\Delta y_{\text{exp}} = 89 \mu\text{m}$ . (b) The quality of focus achievable with the full optical system is shown in Fig. 14b; at the XTM-station and with a photon-energy of 10 keV, the vertical focus size is  $\Delta y_{\text{exp}} = 160 \mu\text{m}$ . These experimental results for the vertical focus are compared with calculations in Table 6, where  $S$ ,  $M1$ ,  $M2$  and  $F$  are the positions along the beamline of the wiggler source, mirror 1, mirror 2 and the focus, respectively, and the vertical magnification for perfect collimation by M1 is given by  $M = -Q/P = -(F - M2)/(M1 - S)$ . In the presence of sagittal focusing, the (FWHM) effect of the vertical aberration of crystal X2 must be included [23]:

$$\Delta y_{\text{sagittal}} = \frac{\Delta\phi^2(p_{X2} + q_{X2})}{8 \sin \theta_X}. \quad (20)$$

For our case (b), the FWHM horizontal beam divergence at 10 keV is  $\Delta\phi = 2.56 \text{ mrad}$  (see Fig. 3), the source–X2 and X2–focus distances are  $p_{X2} = 19.7 \text{ m}$  and  $q_{X2} = 12.7 \text{ m}$ , respectively and  $\theta_X = 11.4^\circ$  is the Bragg angle. The resulting sagittal-focusing aberration contribution is  $\Delta y_{\text{sagittal}} = 134 \mu\text{m}$ . Quadratically adding the source-size, slope-error and sagittal contributions finally yields the theoretical vertical focus size, which, as can be seen in Table 6, is in good agreement with measurement.

Fig. 14a shows the beam spot at 10 keV, near the XTM-station, with flat mirrors and an intermediate setting of the crystal bending. The mirror imperfections and the second-crystal ribs cause strong inhomogeneities in the beam intensity profile, which have serious consequences for full-field imaging experiments such as X-ray microtomography (see also the discussion in Section 6.4). The horizontal FWHM width of the focused beam (Fig. 14b) is  $\Delta x_{\text{exp}} = 430 \mu\text{m}$ , which is comparable to the X2-rib width (400  $\mu\text{m}$ ).

### 6.4. Coherence and effective source size

Although the MS-beamline was not designed for high-coherence, it is interesting to consider this property. The longitudinal and transverse

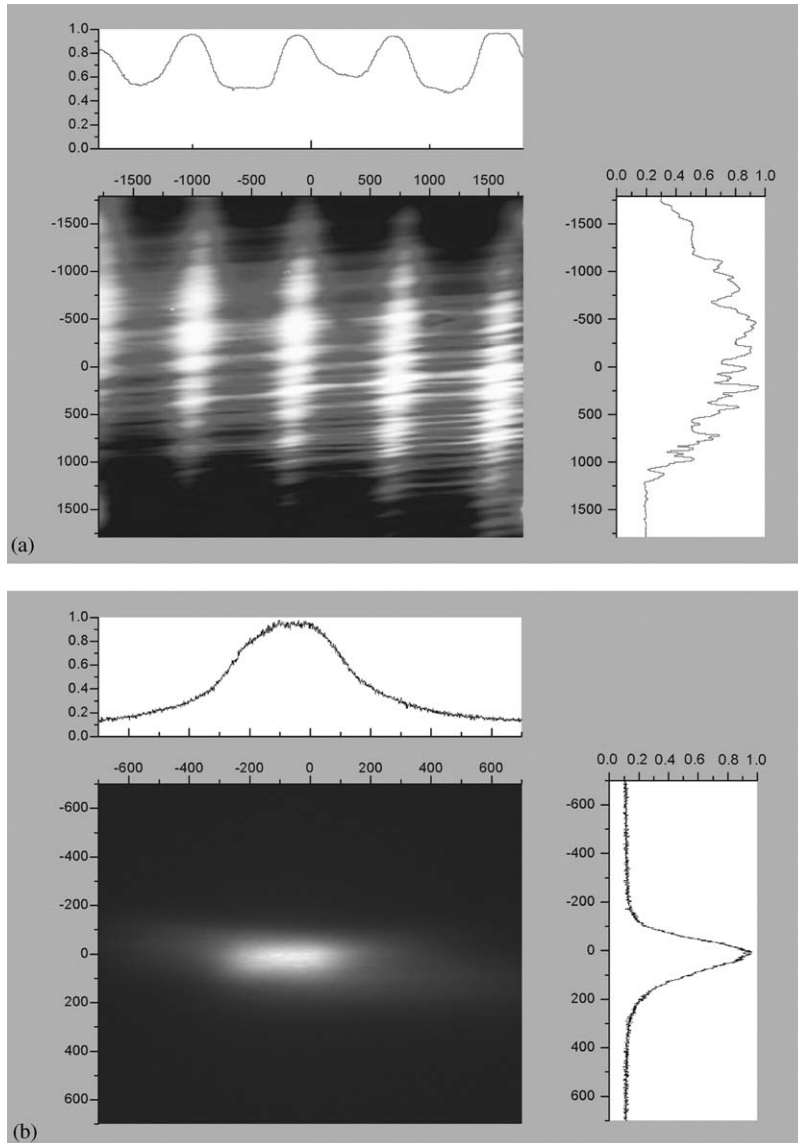


Fig. 14. The focus profile of the monochromatic X-ray beam (10 keV, 32.4 m from the source) with flat mirrors and intermediate sagittal focusing (a) and with optimized focusing (b). The optimal profile widths (FWHM) are 160 (v) × 430 (h) μm. Note the different scales (in μm) between the two figures.

Table 6  
Computation of the FWHM vertical focus size

Situation	$F-S$	$P = M1 - S$	$Q = F - M2$	$M = -Q/P$	$\Delta y_{\text{source}} =  M\Delta s $	$\Delta y_{\text{slope}}$	$\Delta y_{\text{sagittal}}$	$\Delta y_{\text{theory}}$	$\Delta y_{\text{exp}}$
Pink beam focus: $v$	34.83 m	17.57 m	12.83 m	-0.73	55 μm	90 μm	0	106 μm	89 μm
10 keV Focus: $v + h$	32.37 m	17.57 m	10.37 m	-0.59	44 μm	76 μm	134 μm	160 μm	160 μm

coherence lengths [21] are defined as

$$l_{\text{long}} = \frac{\lambda^2}{2\Delta\lambda}, \quad l_{\text{trans}} = \frac{\lambda L}{2\Delta s} \quad (21)$$

where  $L$  is the distance to the source and  $\Delta s$  is the (apparent) source size. Taking  $\Delta\lambda/\lambda \approx 10^{-4}$ , the energy resolution for a Si (111) DCM and at a beam energy of 14 keV, we obtain  $l_{\text{long}} \approx 0.4 \mu\text{m}$ . Using a novel method based on shearing interferometry [27], the transverse (vertical) coherence length of the beamline, at the XTM station (at  $L = 32.37\text{m}$  from the source) and with a photon energy of 14 keV, has been determined to be  $l_{\text{trans}} = 19.2 \mu\text{m}$ . The effective (FWHM) source size is thus  $\Delta s = 75 \mu\text{m}$ . This is much larger than the vertical size of the electron beam from Table 3 (18  $\mu\text{m}$ ), due to scattering in the carbon filter and the Be windows, and is comparable to the contribution to the spot size from the mirror slope-error (see Table 6).

With an approximately parallel beam in the vertical direction, the beam profile at the XTM station (Fig. 14a) shows distinct horizontal stripes, with approximately 100  $\mu\text{m}$  spacing. Since this spacing is much larger than  $l_{\text{trans}}$ , the stripes are not an effect of phase coherence but are rather a geometric effect of mirror imperfections. A truly random slope-error distribution cannot produce such a regular pattern, however—the observed stripes demonstrate the existence of long-range correlated figure errors over the mirror surfaces. It has been found that by inserting a (rotating) diffuse scatterer made of paper after the second mirror (23.0 m from the source), the stripe structure is strongly suppressed. This is due to small-angle scattering in the paper, causing an overlap and hence blurring of the individually scattered stripes. *Note added in proof:* Following discussions with the mirror manufacturer, the strong suspicion has arisen that the long-range correlated figure errors causing the stripes are due to repetitive stepping, by approximately 150 mm, of the lapping tool during polishing.

### 6.5. A note on the beamline length

The issue of beamline length was touched on in Section 5.2; in the light of the preceding

discussions of the focus size and effective source size, we now return to this topic. The following points must be considered: (a) The maximum beamline length compatible with the size of the SLS building is approximately 40 m. (b) Three experimental stations, two of which are dedicated to (high-resolution) diffraction, are serially served. (c) The minimum sample size for diffraction (capillary radius or projected size of a 10 mm sample inclined at  $0.2^\circ$ ) is approximately 50  $\mu\text{m}$ . (d) The best angular resolution required (for high-resolution powder diffraction) is approximately 3  $\mu\text{rad}$  (one third of the Si (111) Darwin width at 30 keV). (e) The effective source size is 75  $\mu\text{m}$ .

With a 75  $\mu\text{m}$  source (approximately equal to the sample size), the 3  $\mu\text{rad}$  divergence criterion dictates a source–experiment distance of at least 25 m; Our PDiff station is at 36.1 m, and our SDiff station is at 40.8 m. We choose approximately 1:1 optics to avoid strong curvatures, remembering that the mirror angles and hence their curvatures are changed with the photon energy; Taking the DCM position (19.6 m) as a reference, the PDiff station sees a magnification of 0.84 and the SDiff station 1.08. The mirror slope-error contribution to the focus spot size grows approximately linearly with the beamline length, effectively imposing a further upper limit in addition to that of the building size. But we have seen in Table 6 that at the PDiff station, the vertical focus is an acceptable 90  $\mu\text{m}$ . For horizontal-scattering experiments at the SDiff station, however, the horizontal focus and the horizontal divergence are larger than desired. Here the solution would be a high-field, perhaps cryogenic, undulator source.

## 7. The experimental stations

As mentioned in the Introduction, the MS Beamline supplies X-rays, alternatively, to three experimental stations: XTM, PDiff and SDiff.

### 7.1. X-ray tomographic microscopy

The XTM station [2], located at the front of the first experimental hutch (sample at 32.37 m), is

mounted on a large optical table, which can be moved on rails into and out of the beam. It consists of a beam conditioner (slits, shutter, ionization chamber), a precise sample positioner, capable of rotating samples with less than  $5\ \mu\text{rad}$  of wobble, and a special-purpose, high-resolution X-ray camera system. This system, a flexible combination of fluorescent screens, microscope objectives and CCD-camera, is capable of  $1\ \mu\text{m}$  resolution and can be translated along the beam, for performing in-line phase-contrast holography. An auxiliary “Bragg magnifier” [28] is also available for ultra-high resolution imaging. In this case, after passing through the sample, the X-ray beam is expanded in both the horizontal and vertical directions by diffraction on asymmetrically cut Si crystals. A typical tomography experiment requires 1000 exposures at different rotation angles and lasts approximately 2 h. The computation of the 3D-reconstruction is performed locally with a dedicated 16-processor cluster, requiring approximately 90 min. Typical XTM investigations include microscopic failure studies of stressed bone biopsies, three-dimensional vascular analyses of prepared brain and lung samples, visualization of fluid transport in microchannels and soils and characterization of fiber-reinforced construction materials.

### 7.2. Powder diffraction

At the rear of the first experimental hutch is the powder diffractometer [3]. Here the beam conditioner includes, in addition, pneumatically insertable filter foils. The diffractometer consists of three coaxial, heavy-duty rotational stages (Eimeldingen, Bath, UK), with a horizontal axis which is perpendicular to the beam. The inner stage provides the  $\omega$ -movement of the sample, and the outer two stages perform  $2\theta$ -movements of two independent detector systems. On the  $2\theta$ -arm of the high-resolution detector are 5 crystals (presently Si (1 1 1)), mounted on a single rotation axis, which are matched to 5 scintillator/photomultiplier detectors on a concentric rotation arm. These components form a 5-fold analyzer–detector, with a  $2^\circ$   $2\theta$ -separation between adjacent channels. A change in incoming photon energy requires a

change, by a single rotation, of the orientation of the 5 crystals, and a rotation and axial translation of the 5-fold scintillator/photomultiplier unit. The advantages of the analyser-detector are: an angular resolution in  $2\theta$  which is given by the Darwin width, rejection of rays not originating from the sample, and rejection of rays with the wrong energy (fluorescence and Compton). The parallel use of 5 individual channels increases counting statistics. The second detector system, the microstrip detector [29], is the result of an in-house development project. A total of 12,000 integrated semiconductor detectors, complete with amplifier, discriminator and counter, are distributed over  $45^\circ$  in  $2\theta$ , with a channel spacing of  $50\ \mu\text{m}$  at a distance of 76 cm, corresponding to  $0.004^\circ$ . In practice, the microstrip detector resolution is determined by the size of the sample (typically a  $200\ \mu\text{m}$  capillary). Although the microstrip detector is susceptible to air and window scattering near the sample, its approximately 1 keV energy resolution allows some degree of inelastic rejection. Each microstrip channel can count up to 1 MHz, with effectively zero dark noise. The entire detector can be read out in several milliseconds, and it is possible to gate the detector for repetitive sampling during periodic changes in the sample environment, e.g., applied electric field, mechanical strain, etc. Three sample environments are available for PDiff users: a  $\text{N}_2$  Cryojet (Oxford Instruments, Oxon, UK) (100–500 K), a He-flow cryostat with integrated spinner (4–300 K) and an electrically heated furnace (300–1700 K). Finally, a Eulerian cradle can be mounted on the sample  $\omega$ -axis, providing  $\chi$  and  $\phi$  rotations for texture and residual-stress measurements and for single-crystal investigations.

### 7.3. Surface diffraction

The surface diffraction station is situated in a separate experimental hutch at the end of the beamline and is equipped with a similar beam conditioner to that for PDiff. The heart of the SDiff station is a large diffractometer of the “2+3” design [30], built by Newport-Microcontrole, Beaune la Rolande, France. The diffractometer is specialized for glancing-incidence

investigations of planar samples (typical size:  $10 \times 10 \text{ mm}^2$ ), which are generally enclosed in an experiment-specific environmental chamber. The sample itself is rigidly mounted on a “hexapod” (Physik Instrumente, Karlsruhe, Germany), which allows three high-precision rotations and translations. The diffractometer supports two measurement geometries: “horizontal”, with the hexapod axis vertical and the sample plane horizontal, or “vertical”, with the hexapod axis horizontal and the sample plane vertical. Possibilities for environmental chambers include a “baby chamber”, which is mounted directly on the hexapod, either in the horizontal or vertical geometry, and a “heavy chamber”, which is mounted on one of the large rotation tables, with a flexible rotational vacuum feedthrough between the vertical sample and the hexapod. The massive detector arm of the diffractometer permits the use of various detector systems, including a scintillator–photomultiplier combination in conjunction with a graphite crystal analyser, a commercial scintillator–CCD camera combination and an in-house-developed “pixel detector” [31]. The last mentioned, with  $366 \times 157$  pixels of  $200 \times 200 \mu\text{m}^2$  area and mounted 1200 mm from the sample, has become the workhorse of the station. Like the microstrip detector at the diffraction station, the pixel detector brings the advantages of negligible dark noise, high counting rate per pixel and approximately 1 keV energy resolution. Several “in situ” environmental chambers have been constructed for the station, including a heavy chamber for pulsed-laser deposition epitaxy [4]. A compact He-refrigerator, allowing sample temperatures in the range 10–300 K, is also available.

#### 7.4. Miscellaneous aspects

Changeovers from one experimental station to another generally involve mounting or dismantling an evacuated beam-pipe and realigning the optics, requiring approximately 30 min. Radiation shielding of the optics and experimental stations is provided by massive lead hutches. The optics hutch has 10–65 mm of lead, depending on the location, and the experimental hutches have 2 mm.

A “local access control” (LAC) safety system, requiring a hutch search prior to locking, has been implemented by the PSI staff.

The beamline comprises a large number of stepping motors, actuators, and sensors, which need to be controlled and monitored. Three levels of controls are incorporated: Personal safety is guaranteed by the LAC-system. The “machine interlock system”, responsible for the integrity of the storage-ring, controls front-end components with a direct impact on synchrotron operations. Finally, an “experimental protection system” monitors the beamline optics. The entire SLS is controlled using the “EPICS” software [32], which also provides the basis for beamline and instrument control. On top of EPICS, graphical-user-interfaces have been created for performing particular functions, such as changing the beamline photon energy or making an “on-the-fly” powder-diffraction measurement, with continuous detector rotation. Finally, the “spec” software package [33] can be used for high-level control of the experimental stations.

## 8. Summary and conclusions

The beamline design and commissioning process can be summarized as follows: The W61 minigap wiggler is very successful, reliably delivering the predicted spectral flux density. Although detailed numerical models of wiggler radiation exist, the simple description of Tatchyn was found to be both accurate and simple to use. A novel rotating filter, based on glassy-carbon material in the shape of a cup, has proven to be a practical solution of the problem of removing the soft X-ray flux at a hard X-ray wiggler beamline at an intermediate-energy storage-ring. The optical beamline components, thanks to their high-quality construction and accurate placement, perform as predicted, producing almost the predicted photon flux over the entire design energy range and into the predicted spot size. The theoretical energy resolution for monochromator crystals has also been achieved. The possibility to remove the monochromator crystals to make

polychromated “pink” beam has proven to be useful, particularly during alignment. Also useful is the possibility to independently set the monochromator energy and the mirror angles. The beamline alternatively serves three experimental stations, and because of rational design, diagnostics and good control software, it is possible to change from one station to another in approximately 30 min. In-house developments in one- and two-dimensional semiconductor detector systems have opened new possibilities for powder and surface diffraction experiments, and the realization of a two-dimensional Bragg-magnifier greatly improves the spatial resolution in tomography experiments.

Problems in the beamline design and performance include a long-range correlated figure-error of the mirrors and the ribbed structure of crystal X2, both of which cause a severely inhomogeneous unfocused beam profile. This is a drawback for imaging experiments such as X-ray microtomography. It came as a surprise that the density of the Rh mirror coating is reduced by 30% compared to bulk, but this fact had no severe consequences. The TORII thermal compensation system for crystal X1 is about at its limit with the thermal load at the MS-beamline. A significant part of the missing flux is attributed to inaccurate thermal-bump compensation, and the system requires sensitive adjustment for large changes in monochromator energy. An unavoidable turbo-molecular pump on the DCM tank produces noticeable vibrations, particularly for settings where the two crystals are close together, implying a small moment of inertia of the main rotation stage. Scattering in the rotating carbon filter and the Be vacuum windows increases the effective source size by a factor of four, to the disadvantage of experiments requiring a high lateral coherence. We do not presently understand the low intensity of the second and third harmonic radiation, but such radiation is generally undesirable. A major drawback for experiments requiring high brightness is the large (2.5 mrad) horizontal divergence of the beam. This is the price one pays for a wiggler source, and a future beamline upgrade may include a short-period in-vacuum undulator.

## Acknowledgements

We would like to acknowledge the helpful assistance of our colleagues: Essential during the beamline design phase were discussions with W. Drube, J. Heuer and H. Schulte-Schrepping, of HASYLAB, Hamburg and P. Berkvens and A. Freund, of ESRF, Grenoble. Competent advice and technical assistance was provided by many staff members at PSI, in particular by M. Böge, Ch. David, U. Flechsig, G. Heidenreich, R. Hugi, S. Hunt, R. Krempaska, J. Krempasky, M. Kropf, F. Pfeiffer, M. Spielmann, U. Staub, J.F. van der Veen and D. Vermeulen.

## Appendix A. X-ray optical constants for selected materials

Knowledge of the photon-energy-dependent complex scattering function  $F_1(E) + iF_2(E)$  of a material allows one to compute other functions of interest.

(a) The complex index of refraction of a material for X-rays is given by

$$\begin{aligned} n &\equiv 1 - \delta - i\beta \\ &= 1 - \frac{2\pi r_0 \rho_a}{k^2} (F_1 + iF_2) \end{aligned} \quad (\text{A.1})$$

where  $\rho_a$  is the atomic density,  $r_0 = e^2 / (4\pi\epsilon_0 mc^2) = 2.82 \times 10^{-15}$  m is the classical electron radius and  $k = 2\pi/\lambda$  is the radiation wave-vector.

(b) The inverse absorption length is given by

$$\mu = 2\beta k = \frac{4\pi r_0 \rho_a F_2}{k}. \quad (\text{A.2})$$

Numerical values for these and other functions are available from the internet [35]. Table A1 presents fitted parameter values for the indicated functions, according to the approximate energy dependence:

$$\text{Function}(E) = \exp[A + B \ln E + C \ln^2 E] \quad (\text{A.3})$$

(unless otherwise stated), where  $E$  is the photon energy in keV.

Table A1

Coefficients for an approximate expression (Eq. (A.3) unless otherwise noted) for atomic scattering factors and inverse absorption length for various materials

Element/material	Atomic density $\rho_a$ (mol/cm <sup>3</sup> )	Function	$E_{\min}$ (keV)	$E_{\max}$ (keV)	$A$	$B$	$C$	Accuracy
Al	0.100	F2	5	30	2.26	-1.594	-0.0815	0.25%
Ar	0.0000446	F2	5	30	3.26	-1.414	-0.0959	0.8%
Be	0.202	F2	3	30	-1.96	-2.079	-0.0426	1%
C (graphite)	0.175	F2	3	30	-0.438	-1.820	-0.0958	1.5%
Mo	0.106	F2	3	20.0	4.24	-1.386	-0.0770	1.3%
			20.0	30	4.167	-0.3284	-0.2084	0.08%
N (atoms)	0.0000893	F2	5	30	0.279	-1.922	-0.0629	1.5%
Polyimide (Kapton <sup>®</sup> )		$\mu$ ( $\mu\text{m}^{-1}$ )	5	16	-0.0803	-3.654	0.139	2.5%
Rh	0.121	F1	5	23.2	$F1 = 46.2 - 0.135 * E$			
		F1	23.2	30	$F1 = 37.5 + 0.241 * E$			
		F2	5	23.2	4.91	-1.740	0	
		F2	23.2	30	6.37	-1.611	0	$\Delta R/R < 4\%$
Si	0.0833	F2	5	30	2.53	-1.590	-0.0780	0.25%
		F2	5	120	3.527	-2.1514	0	33%

## Appendix B

“Mathematica<sup>®</sup>” program for the beamline flux.

### Beamline Flux Calculation

Needs[“Graphics‘Graphics’”]

Mathematical functions. G1 (Refs. [10,34]) and probability integral

```
(G1[y_] := Exp[-0.4333
  -0.6754*Log[y]
  -0.4647*Log[y]^2
  -0.1672*Log[y]^3
  -0.04877*Log[y]^4
  -0.008866*Log[y]^5
  -0.0006711*Log[y]^6];
ProbFcn[x_] := Erf[x/Sqrt[2]]);
```

### Physical constants

```
(r0 = 2.817*10^-15; Avagadro = 6.022*10^23; coul = 1.602*10^-16;
hce = 1.23984*10^-9;
factmu = 2*r0*Avagadro*hce; factn = r0*10^6*Avagadro*hce^2/(2*Pi);)
```

*SLS machine parameters*

```
(Eel = 2.4; Iel = 0.3; gamma = Eel/0.000511;)
```

*W61 wiggler parameters and field profile*

```
(gap = 8; eta = -0.163; WigglerLength = 2000;
PeriodLength = 60.5; Npoles = 2*WigglerLength/PeriodLength;
Bmax[gap_] := 3.2443 - 0.22386*gap + 0.0068182*gap^2 -
0.00009972*gap^3 + 0.00000056173*gap^4;
Bn = (Bmax[gap]/(1-eta))*{1, 0, eta, 0};
B[z_] := Sum[Bn[[2*n-1]]*Sin[2*(2*n-1)*Pi*z/PeriodLength], {n, 1, 2}];)
```

*Wiggler spectral flux density (ph/s/0.1%bw) in a horiz. aperture Dphi (from Ref. [8])*

```
(Kn = Table[0.934*0.1*PeriodLength*Bn[[m]]/m, {m, 1, 4}];
KT = Sum[Kn[[m]], {m, 1, 4}];
PsiM = 1000*(KT/gamma)/Sqrt[1-(KT/gamma)^2];
Ec[z_] := 0.665*Eel^2*B[z];
Ec0 = Ec[PeriodLength/4];
dsum[z_] := Sum[Kn[[m]]*Cos[2*m*Pi*z/PeriodLength], {m, 1, 4}];
theta[z_] := 1000*ds/Sqrt[gamma^2-ds^2]/.ds->dsum[z];
FluxZ[EkeV_, zmax_] := (2*Npoles*1.1*10^13*1000*Iel*EkeV/
Eel^2)*0.001*NIntegrate[(Ec[z]
/EkeV)*G1[EkeV/Ec[z]], {z, zmax, PeriodLength/4}];
IFract[EkeV_, Dphi_] := (zmax = z/.FindRoot[theta[z]
== Dphi, {z, 0.8*PeriodLength/4}]; Return
[FluxZ[EkeV, zmax]]);)
```

*Wiggler spectral flux density (ph/s/0.1%bw; vertical profile is Gaussian)*

```
(FWHMV[EkeV_] := (2.35*1000/gamma)*0.58/Sqrt[EkeV/Ec0];
SpectralFluxAperture[EkeV_, apertureV_, apertureH_] :=
IFract[EkeV, apertureH/2]*ProbFcn[apertureV*2.35/(2*FWHMV[EkeV])];
SpectralFluxAperture[10, 4, 4])
```

$1.3219 \times 10^{15}$

*Front-end aperture (mrad) and filter and window thicknesses (micrometers)*

```
(aperV = 0.23; aperH = 2.5; dC = 2000; dBe = 500;)
```

*Sigradur filter and window transmission*

```
(muC[EkeV_] :=
factmu*(0.118/EkeV)*Exp[-0.438-1.820*Log[EkeV]-0.0958*Log[EkeV]^2];)
```

```

muBe[EkeV_] := factmu*(0.202/EkeV)*
  Exp[-1.96-2.079*Log[EkeV]-0.0426*Log[EkeV]^2];
TransC[EkeV_] := Exp[-muC[EkeV]*dC];
TransBe[EkeV_] := Exp[-muBe[EkeV]*dBe];)

```

### Power in front-end (kW)

```

(PWiggler = coul*NIntegrate[SpectralFluxAperture[EkeV, 4, 4],
  {EkeV, 0.01, 50}];
Paper = coul*NIntegrate[SpectralFluxAperture[EkeV, aperV, aperH],
  {EkeV, 0.01, 50}];
PabsC = coul*NIntegrate[
  (1-TransC[EkeV])*SpectralFluxAperture[EkeV, aperV, aperH], {EkeV, 0.01,
  50}];
PabsBe = coul*NIntegrate[(1-TransBe[EkeV])*TransC[EkeV]*Spectral
FluxAperture [
  EkeV, aperV, aperH], {EkeV, 0.01, 50}]; {PWiggler, Paper, PabsC, PabsBe})
{5.57121, 2.80208, 1.6092, 0.0255043}

```

### Rh-optical constants (with reduced density)

```

(f1Rh[EkeV_] := N[46.2-0.135*EkeV]/;EkeV<=23.2;
f1Rh[EkeV_] := N[37.5+0.241*EkeV]/;EkeV>23.2;
f2Rh[EkeV_] := N[Exp[4.9-1.740*Log[EkeV]]]/;EkeV<=23.2;
f2Rh[EkeV_] := N[Exp[6.37-1.611*Log[EkeV]]]/;EkeV>23.2;
delta[EkeV_] := factn*((8.9*0.121/12.4)/EkeV^2)*f1Rh[EkeV];
beta[EkeV_] := factn*((8.9*0.121/12.4)/EkeV^2)*f2Rh[EkeV];)

```

### Mirror reflectivity (angle in mrad)

```

(thetaCritical[EkeV_] := N[1000*Sqrt[2*delta[EkeV]]];
afact[EkeV_, thetaM_] := thetaM/thetaCritical[EkeV];
hfact[EkeV_, thetaM_] := afact[EkeV, thetaM]^2+Sqrt[(afact[EkeV, thetaM]
^2-1)^2+(beta[EkeV]/delta[EkeV])^2];
Refl[EkeV_, thetaM_] := N[(hfact[EkeV, thetaM]-afact[EkeV, thetaM]*Sqrt[2*
(hfact[EkeV, thetaM]-1)])/(hfact[EkeV, thetaM]+afact[EkeV, thetaM]*Sqrt[2*(hfact[EkeV,
thetaM]-1)])];)

```

### Mirror coordinates (m), empirically-optimized angle and aperture (mrad)

```

(distM1 = 17.566; LengthM1 = 0.8; thetaMemp[EkeV_] := 62.218*10^-1.0969/;
EkeV<=10;
thetaMemp[EkeV_] := 62.218*EkeV^-1.0969/; EkeV>10;
ApertureM1[thetaM_] := thetaM*LengthM1/distM1;)

```

*Absorbed and reflected power at mirror 1 (kW) as a function of photon energy setting*

```

(PabsM1[EkeVset_] :=
  coul*NIntegrate[(1-Refl[EkeV, thetaMemp[EkeVset]])*TransBe[EkeV]*
    TransC[EkeV]*SpectralFluxAperture[EkeV, ApertureM1[thetaMemp[EkeVset]],
    aperH], {EkeV, 0.01, 50}];
PrefM1[EkeVset_] := coul*NIntegrate[Refl[EkeV, thetaMemp[EkeVset]]*TransBe
[EkeV]*
  TransC[EkeV]*SpectralFluxAperture[EkeV, ApertureM1[thetaMemp[EkeVset]],
  aperH],
  {EkeV, 0.01, 50}]; {PabsM1[10], PrefM1[10]})

{0.875114, 0.28375}

```

*Crystal 1 coordinates (m), Bragg angle and aperture (mrad)*

```

(distX1 = 19.537; LengthX1 = 0.07; thetaBragg[EkeV_] := 1000*ArcSin[1.976/
EkeV];
ApertureX1[EkeV_] :=
  Min[ApertureM1[thetaMemp[EkeV]],
  1000*Sin[thetaBragg[EkeV]/1000]*LengthX1/distX1];)

```

*DCM-Transmission and monochromatic flux (ph/s)*

```

(DCMTrans[EkeV_] := 0.1396-1.622*EkeV^-1.963;
Flux[EkeV_] := DCMTrans[EkeV]*Refl[EkeV, thetaMemp[EkeV]]^2*TransC[EkeV]*
  TransBe[EkeV]*SpectralFluxAperture[EkeV, ApertureX1[EkeV], aperH];
{Flux[10], Flux[20], Flux[30]})

```

```

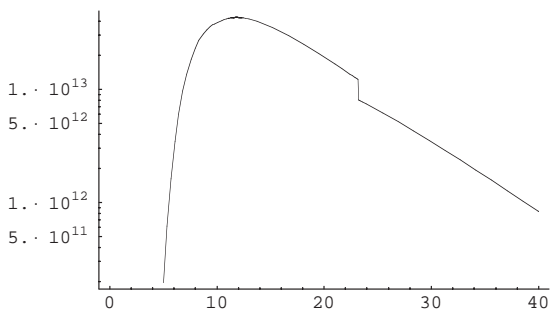
{3.82962 × 1013, 1.92359 × 1013, 3.43608 × 1012}

```

```

LogPlot[Flux[EkeV], {EkeV, 5, 40}]

```



### Appendix C. Mirror and crystal focusing

For a glancing incidence angle  $\theta$ , the meridional (vertical) and sagittal (horizontal) focal lengths of a curved mirror (radius  $R$ ) are given by

$$f_{\text{meridional}} = \frac{R_{\text{meridional}} \sin \theta}{2},$$

$$f_{\text{sagittal}} = \frac{R_{\text{sagittal}}}{2 \sin \theta}. \quad (\text{C.1})$$

With a source–mirror distance  $p$  and a mirror–image distance  $q$ , the “lensmaker equation”  $1/f = 1/p + 1/q$  yields the “Coddington” equations for meridional and sagittal focusing [17]:

$$R_{\text{meridional}} = \frac{2}{\sin \theta} \left( \frac{pq}{p+q} \right),$$

$$R_{\text{sagittal}} = 2 \sin \theta \left( \frac{pq}{p+q} \right). \quad (\text{C.2})$$

At the MS-beamline, the second DCM crystal provides sagittal focusing and hence must be bent to a radius  $R_{\text{sagittal}}$ , with  $p$  equal to the source–X2 distance and  $q$  equal to the X2–focus distance. Normally, the two beamline mirrors have the same incidence angle, the first mirror is collimating ( $q$  infinite) and the second mirror focuses a parallel incident beam ( $p$  infinite). Because it is occasionally necessary to deviate from this situation, we found it useful to derive a focusing condition for the general case of two meridionally focusing mirrors. The geometry is shown in Fig. 15, where the source is at the far left, and the image is at the far right. We define the “relative” curvature radii  $r_i$  as the radii divided by their “normal” values  $R_i^\infty$ :

$$r_1 \equiv \frac{R_1}{R_1^\infty}, \quad R_1^\infty = \frac{2L_1}{\sin \theta_1}$$

$$r_2 \equiv \frac{R_2}{R_2^\infty}, \quad R_2^\infty = \frac{2L_2}{\sin \theta_2}. \quad (\text{C.3})$$

By successive applications of the lensmaker equation, we obtain the two-mirror focusing condition:

$$\frac{L_1}{(1/r_1) - 1} + \frac{L_2}{(1/r_2) - 1} = D. \quad (\text{C.4})$$

This equation was useful during the mirror-curvature measurements described in Section 5.2.1.

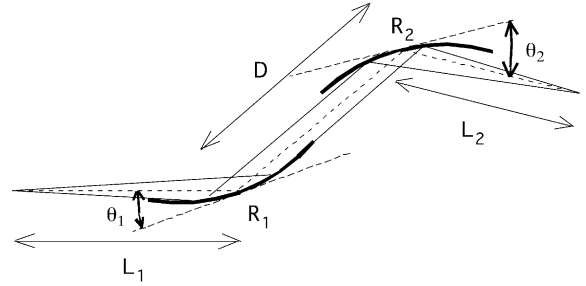


Fig. 15. A schematic diagram for two-mirror focusing. The source is at the left and the focus at the right.

### References

- [1] M. Böge, et al., Sixth European Particle Accelerator Conference (EPAC 98), Stockholm, 1998, pp. 623–625.
- [2] M. Stapanoni, et al., Nucl. Instr. and Meth. A 491 (2002) 291.
- [3] F. Gozzo, et al., J. Alloys Compounds 362 (2004) 206.
- [4] P.R. Willmott, et al., Appl. Surf. Sci., in press.
- [5] G. Ingold, Th. Schmidt, to be published.
- [6] K. Halbach, J. Phys. C1 44 (1983) 211.
- [7] E.M. Takhtenberg, E. Gluskin, S. Xu, Rev. Sci. Instr. 66 (1995) 1809.
- [8] R. Tatchyn, Nucl. Instr. and Meth. A 336 (1993) 361.
- [9] G. Brown, K. Halbach, J. Harris, H. Winick, Nucl. Instr. and Meth. 208 (1983) 65.
- [10] K-J Kim, in: M. Month, M. Dienes (Eds.), Physics of Particle Accelerators, AIP Conference Proceedings, vol. 184, 1989, pp. 565–633.
- [11] 6GeV Synchrotron X-ray Source Conceptual Design Report, Supplement A, LS-52 (March 1986), Argonne National Laboratory.
- [12] [http://www.esrf.fr/machine/groups/insertion\\_devices/Codes/SRW/srwindex.html](http://www.esrf.fr/machine/groups/insertion_devices/Codes/SRW/srwindex.html).
- [13] W.B. Peatman, K. Holldack, J. Synchrotron Radiat. 5 (1998) 639.
- [14] HTW GmbH, Thierhapputen, Germany.
- [15] A. Allemandi, et al., Sincrotrone Trieste internal report ST/S-TN-93/59, 1993.
- [16] P. Berkvens, Swiss Light Source internal report SLS-TM September 1999, 1999.
- [17] J. Susini, Opt. Eng. 34 (1995) 361.
- [18] H. Schulte-Schrepping, G. Materlik, J. Heuer, T. Teichmann, Rev. Sci. Instr. 66 (1995) 2217.
- [19] A.K. Freund, et al., SPIE 3448 (1998) 144.
- [20] S. Takagi, J. Phys. Soc. Jpn. 26 (1969) 1239; D. Taupin, Acta Crystallogr. 23 (1967) 23.
- [21] J. Als-Nielsen, D. McMorrow, Elements of Modern X-ray Physics, Wiley, New York, 2001.
- [22] <http://yagi.spring8.or.jp/ic.html>.
- [23] C. Schulze, G. Heidenreich, H. Auderset, D. Vermeulen, A.K. Freund, Proceedings SPIE 3448 (1998) 156.

- [24] J.J. DeMarco, R.J. Weiss, *Phys. Rev.* 137 (1965) A1869.
- [25] EXAFS Materials, Danville, CA, USA.
- [26] J. Bahrtdt, U. Flechsig, F. Senf, *Rev. Sci. Instr.* 66 (1995) 2719.
- [27] Ch. David, F. Pfeiffer, to be published.
- [28] M. Stampanoni, et al., *Appl. Phys. Lett.* 82 (2003) 2922.
- [29] B. Schmitt, et al., *Nucl. Instr. and Meth. A* 501 (2003) 267.
- [30] E. Vlieg, *J. Appl. Crystallogr.* 31 (1998) 198.
- [31] E.F. Eikenberry, et al., *Nucl. Instr. and Meth. A* 501 (2003) 260.
- [32] <http://www.aps.anl.gov/epics/>.
- [33] <http://www.certif.com/>.
- [34] V.O. Kostroun, *Nucl. Instr. and Meth.* 172 (1980) 371.
- [35] [www-cxro.lbl.gov/](http://www-cxro.lbl.gov/) and [physics.nist.gov/PhysRefData/](http://physics.nist.gov/PhysRefData/).